RESEARCH

Derived Electron Densities from Linear Polarization Observations of the Visible-Light Corona During the 14 December 2020 Total Solar Eclipse

Liam Edwards[1] · **Kaine A. Bunting[1]** · **Brad Ramsey[1]** · **Matthew Gunn[1]** · **Tomos Fearn[2]** · **Thomas Knight[1]** · **Gabriel Domingo Muro[1,3]** · **Huw Morgan[1]**

Abstract

A new instrument was designed to take visible-light (VL) polarized brightness (*pB*) observations of the solar corona during the 14 December 2020 total solar eclipse. The instrument, called the *Coronal Imaging Polarizer* (CIP), consisted of a 16 MP CMOS detector, a linear polarizer housed within a piezoelectric rotation mount, and an f-5.6, 200 mm DSLR lens. Observations were successfully obtained, despite poor weather conditions, for five different exposure times (0.001 s, 0.01 s, 0.1 s, 1 s, and 3 s) at six different orientation angles of the linear polarizer (0°, 30°, 60°, 90°, 120°, and 150°). The images were manually aligned using the drift of background stars in the sky and images of different exposure times were combined using a simple signal-to-noise ratio cut. The polarization and brightness of the local sky were also estimated and the observations were subsequently corrected. The *pB* of the K-corona was determined using least-squares fitting and radiometric calibration was done relative to the *Mauna Loa Solar Observatory* (MLSO) K-Cor *pB* observations from the day of the eclipse. The *pB* data was then inverted to acquire the coronal electron density, n_e, for an equatorial streamer and a polar coronal hole, which agreed very well with previous studies. The effect of changing the number of polarizer angles used to compute the *pB* is also discussed and it is found that the results vary by up to $\approx 13\%$ when using all six polarizer angles versus only a select of three angles.

Keywords Eclipse observations · Polarization · Optical · Instrumentation and data management · Spectrum · Visible

1. Introduction

A total solar eclipses (TSE) provides a unique opportunity to observe the visible-light (VL) corona down to the solar limb for a few minutes during totality, and allow continuous observations from the limb out to several solar radii. Not only does the Moon block out the solar

✉ L. Edwards
lie6@aber.ac.uk

[1] Department of Physics, Aberystwyth University, Ceredigion, Cymru, SY23 3BZ, UK

[2] Department of Computer Science, Aberystwyth University, Ceredigion, Cymru, SY23 3DB, UK

[3] Space Radiation Lab, California Institute of Technology, Pasadena, CA, 91125, USA

disk, but it also lowers the local sky brightness along the eclipse path, which makes it perfect for observing the significantly fainter corona (Lang, 2010). This lower coronal region (< 2 R$_\odot$) is the origin of the solar wind and is therefore crucial to observe in order to better understand how the solar wind is formed and accelerates to supersonic speeds (Habbal, 2020; Strong et al., 2017; McComas et al., 2007). TSEs have been used to obtain valuable information about a variety of solar phenomena, including coronal streamers (Pasachoff and Rušin, 2022), coronal mass ejections (CMEs) (Boe et al., 2021c; Filippov, Koutchmy, and Lefaudeux, 2020; Koutchmy et al., 2004), coronal holes (Pasachoff and Rušin, 2022), plasma flows (Sheeley and Wang, 2014; De Pontieu et al., 2009), prominences (Jejčič et al., 2014), and coronal jets (Hanaoka et al., 2018). Physical properties of the coronal plasma have also been studied extensively during TSEs; typically, temperature, density, and velocity (Del Zanna et al., 2023; Muro et al., 2023; Bemporad, 2020; Reginald et al., 2014; Habbal et al., 2011, 2010; Reginald, Davila, and Cyr C, 2009; Habbal et al., 2007).

A coronagraph is required in order to observe the VL corona outside of a total solar eclipse. First designed by Bernard Lyot in the 1930s (Lyot and Marshall, 1933), it consists of a telescope with an opaque disk that is positioned to block out the bright disk of the Sun. This is crucial because the photosphere is $\approx 10^6$ times brighter than the corona itself. In fact, the Earth's sky is also much brighter than the corona – of the order $\approx 10^5$ times brighter at 20 R$_\odot$ – therefore, any ground-based coronagraph, such as the *COronal Solar Magnetism Observatory's* (COSMO) *K-Coronagraph* (K-Cor: Hou, de Wijn, and Tomczyk, 2013), is affected by the Earth's own atmosphere. To overcome this issue, several space-based coronagraphs have been launched in recent decades, for example, the *Large Angle Spectrometric Coronagraph* (LASCO: Brueckner et al., 1995) onboard the *Solar and Heliospheric Observatory* (SOHO: Domingo, Fleck, and Poland, 1995) and the *Sun-Earth Connection Coronal and Heliospheric Investigation* (SECCHI: Howard et al., 2008) COR1/2 instruments onboard the *Solar Terrestrial Relations Observatory* (STEREO: Kaiser et al., 2008). However, despite the unprecedented access to the corona they have given the field of solar physics, there is still a fundamental issue for any type of coronagraph to overcome, which is the stray light resulting from the diffraction of incoming light at the occulter edge. In order to mitigate this, most occulters will block not only the solar disk but also a portion of the very lower solar corona – out to around 1.5 R$_\odot$ for internally occulted coronagraphs (Verroi, Frassetto, and Naletto, 2008). One way to circumvent this issue is to increase the distance between the detector and the occulter, which is possible to achieve in space by the use of formation-flying cube satellites (e.g., the Association of Spacecraft for Polarimetric and Imaging Investigation of the Corona of the Sun, ASPIICS: Lamy et al., 2010), however, these type of instruments are still in their infancy. As a result, observations of the inner corona during a TSE are unmatched in the VL regime.

The VL corona is composed of light from several different sources, primarily from the scattering of photospheric light by free electrons in the corona and dust in the interplanetary plane, termed the K- and F-corona, respectively. In the case of the K-corona, the scattering process – known as Thomson scattering – produces a strongly tangentially polarized component to the total VL brightness (for an indepth overview of this mechanism see Inhester, 2015), whereas the F-corona is considered to be unpolarized below ≈ 3 R$_\odot$ (Morgan and Habbal, 2007). As a result, observing the VL corona below this height with a linear polarizer during a TSE can be considered to be a measurement of the K-coronal brightness only. There are also other types of brightness contributions to the total coronal brightness, namely the E-corona (emission) that consists of spectral-line emission from highly ionized atoms, but these are considered to be negligible for the purposes of this work. The K-coronal brightness component, B_K, represents the structure and amount of coronal plasma irrespective of

its temperature, unlike EUV or X-ray observations. The K-coronal component of the polarized brightness (pB_k) gives the electron density (n_e) that is calculated using an inversion method first developed by van de Hulst (1950) and later improved upon by Hayes, Vourlidas, and Howard (2001) and Quémerais and Lamy (2002). Equation 1 describes the relationship between the polarized brightness of the K-corona and the electron density that is used to acquire the electron density from the TSE images:

$$pB_k \propto \int_{\text{LOS}} n_e(r) \cdot G(s, \rho) \, ds, \tag{1}$$

where G is a geometrical weighting function, ρ is the distance between the Sun and the intercept between the line-of-sight (LOS) and the plane-of-sky (POS), and s is the distance between the intercept point on the POS and an arbitrary point in the corona along the LOS (see Figure 1 in Quémerais and Lamy, 2002 for more detail). This is a well-established technique and several studies have used this inversion of pB to obtain coronal electron densities (e.g. Liang et al., 2022; Bemporad, 2020; Skomorovsky et al., 2012; Hayes, Vourlidas, and Howard, 2001; Raju and Abhyankar, 1986; Saito, Poland, and Munro, 1977). Several studies have also been conducted attempting to separate the K- and F-components of the solar corona (e.g. Boe et al., 2021a; Fainshtein, 2009; Morgan and Habbal, 2007; Dürst, 1982; Calbert and Beard, 1972). Most of the previous studies involving TSE observations require some level of image processing as a result of several factors – primarily the sharp decrease in brightness with radial height from the Sun. For example, since the Moon and the Sun move relative to each other with respect to the background stars, all TSE images need to be coaligned and there are a number of different methods that can be used to do this. One of the most common of these methods over the past decade or so has been to use a modified phase-correlation technique by Druckmüller (2009), whereas others have used more manual methods such as using the drift of background stars as they move relative to the TSE (Bemporad, 2020). There are also many different image-processing techniques that have been developed to better reveal various structures and phenomena (Patel et al., 2022; Qiang et al., 2020; Morgan and Druckmüller, 2014; Druckmüller, 2013; Byrne et al., 2012; Druckmüllerová, Morgan, and Habbal, 2011). The outline of this paper is as follows. Section 1.1 describes the 2020 TSE in more detail. Section 2 summarizes the design of the instrument (2.1), and the calibrating, processing, coaligning, and inversion to derive the coronal electron densities (Sections 2.2.3 – 2.2.7). Section 3 presents the results of the study, with Sections 4 and 5 disseminating and concluding the results of this work, respectively.

1.1. 14 December 2020 Total Solar Eclipse

The TSE on 14 December 2020 was observed by a team from Aberystwyth University at a site in Neuquén province, Argentina. The observation site was located at $39° \, 42' \, 40.4''$ S, $70° \, 23' \, 57.6''$ W, and an altitude of ≈ 1082 m (3550 ft). Totality lasted ≈ 129 s with the time of maximum eclipse at 13:07:58 local time (16:07:58 UTC) and the apparent altitude of the Sun above the horizon was $\approx 75°$. The weather conditions at the time of observation were not optimal with intermittent cloud cover and very strong gusts of up to 70 km/h that resulted in a lot of airborne dust. Furthermore, a small, wispy cloud passed across the Sun's disk for ≈ 12 s. This had an adverse effect on the quality of the data but, despite the conditions, the data captured during totality were still usable. Figure 1 shows the location of the observation site (white marker) along with the cloud cover at approximately the time of the eclipse. During this eclipse, a CME had erupted from the eastern limb of the Sun ≈ 110 min before totality, providing a truly unique opportunity to study CME dynamics
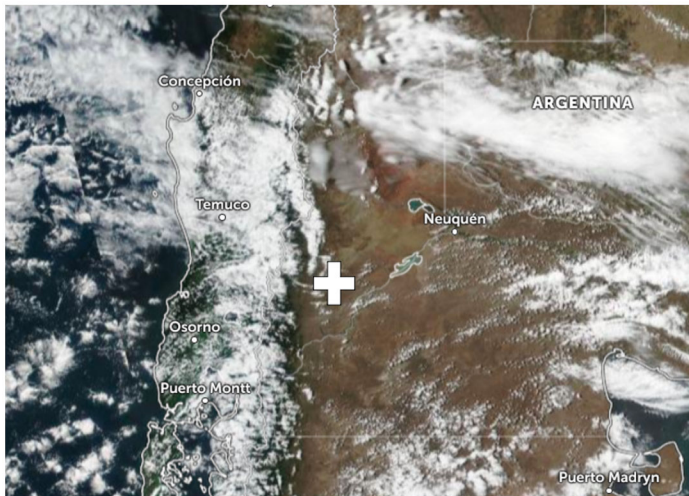
Figure 1   Satellite image of cloud cover above the observation site in Neuquén province, denoted by the white marker, taken at approximately 13:30 local time (Credit: Zoom Earth).

right down to the solar limb. The LASCO CME catalog (Gopalswamy et al., 2009) states that the CME first appeared in the C2 field-of-view (FOV) at 15:12:10 UT with an estimated linear speed of 437 km/s, mass of 3×10^{12} kg, and a central position angle of 121°. The CME is discussed in detail by Boe et al. (2021c).

2. Instrument Design and Data Processing

2.1. The Coronal Imaging Polarizer (CIP)

The instrument used to observe the corona during the total solar eclipse was a VL linear polarization imager designed and built at Aberystwyth University. The *Coronal Imaging Polarizer* (CIP) – shown in Figure 3 – was designed to be relatively cheap and simple to build, easy to assemble, and lightweight in order to be able to be relocated quickly on the day of an eclipse if necessary. It consisted of an objective lens, a VL bandpass filter,[1] a linear polarizer[2] housed in a rotating mount,[3] and a CMOS sensor.[4] The objective lens, an f-5.6, 200 mm focal length DSLR lens, can be adjusted to give different fields of view if required. The VL bandpass filter has a center wavelength of 520 nm (denoted by the vertical dashed black line in Figure 2) where transmission is > 90%, and a bandwidth (FWHM) of 10 nm. Since the peak of the Sun's emission is around 500 nm, the filter is well placed to collect the maximum amount of light possible.
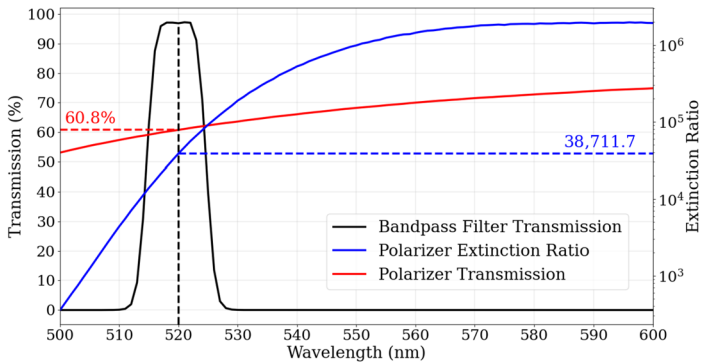
Traditionally, when taking VL polarization observations of the corona, a polarizer is either manually rotated through a set of polarization angles (typically 3 – 5) or several different instruments are set up, each designed to capture the light of a single polarizer orientation

---

[1]https://www.thorlabs.com/thorproduct.cfm?partnumber=FBH520-10.

[2]https://www.thorlabs.com/thorproduct.cfm?partnumber=LPVISC100.

[3]https://www.thorlabs.com/newgrouppage9.cfm?objectgroup_id=12829.

[4]https://www.atik-cameras.com/product/atik-horizon-ii/.

Figure 2 Extinction ratio and transmissions for both the bandpass filter and linear polarizer measured by their respective manufacturers. The dotted horizontal lines correspond to the extinction ratio (blue) and transmission (red) of the polarizer at the center wavelength of the bandpass filter (data from Thorlabs.)
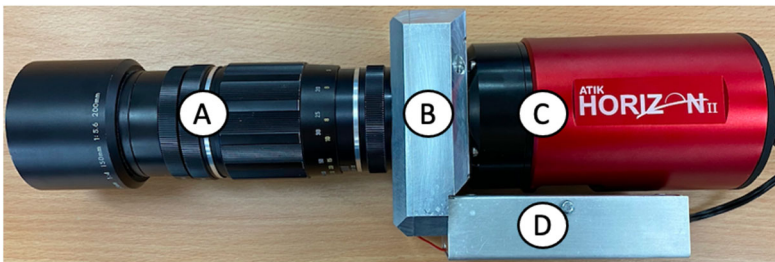
Figure 3 *The Coronal Imaging Polarizer* (CIP) – *A:* f-5.6, 200 mm objective lens. *B:* housing containing the rotation mount, polarizer, and VL filter. *C:* Atik Horizon II 16 MP CMOS camera. *D:* housing for the interface board of the rotation mount.

angle. In contrast, CIP used a piezoelectrically driven rotation mount from Thorlabs to automatically rotate the polarizer through six different polarization angles (0°, 30°, 60°, 90°, 120°, and 150°). The motorized rotation mount allows for 360° rotation with a maximum rotation speed of 430°/s and has an accuracy of ±0.4°, resulting in high precision and fast rotation. The energy requirement of the motor is very low, needing only a maximum of 5.5 V DC input with a typical current consumption of 800 and 50 mA during movement and standby, respectively.

The camera used for CIP (see Figure 3) was the Horizon II – a 16 mega-pixel CMOS camera developed by Atik. It uses the Panasonic MN34230 4/3″ CMOS sensor with a 4644×3506 resolution and has a very low readout noise (≈ 1 e⁻). It is powered by a 12 V 2 A DC input and has a minimum exposure time of 18 μs and unlimited maximum exposure. It is also cooled via an internal fan and can maintain a ΔT of -40 °C, meaning that the camera can still maintain low thermal noise even at high ambient background temperatures. It is a black-and-white camera since using an RGB camera requires extra steps when processing the data (e.g. demosaicking), and the correction and alignment must be done individually for each RGB channel, see Bemporad (2020), for example. In order for the instrument to run in the most efficient way possible, the data-collection process was fully automated. The rotation mount rotates the polarizer to a specific angle, then the camera collects a sequence of images of varying exposure times from $0.001 - 3$ s, then the polarizer is rotated to the next
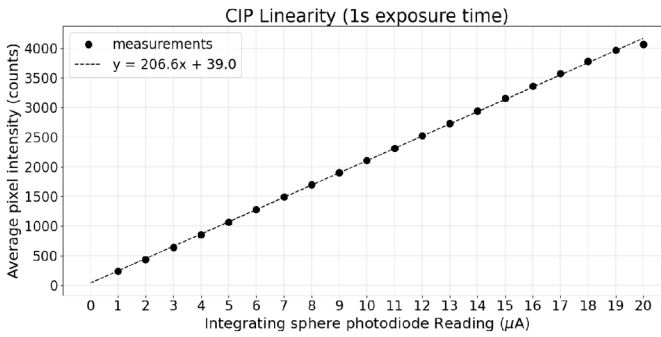
Figure 4 Average pixel intensity as a function of the integrating sphere's photodiode reading (black dots) and the calculated line of best fit (dashed line) giving an R^2 value of 0.99956.

angle, and the camera would run through the same sequence as before, and so on for all six polarization angles. The time taken for one complete cycle of data collection is around 30 s, which resulted in two full datasets and a third partial dataset.

2.2. Data Processing

2.2.1. Linearity

The response of the imaging sensor to incoming light intensity is measured by using an integrating sphere, where the level of illumination in the sphere is measured by a photodiode (in Amps). The integrating sphere is not calibrated to give the light levels in SI units but it is linear, so if the photodiode current doubles the light level in the sphere is doubled. The illumination of the sphere was gradually increased by 1 μA until it reached the saturation point. Five measurements were taken and an average intensity was calculated for each photodiode reading. Figure 4 presents the results of this linearity test and it clearly shows that the sensor used in CIP had a linear response. The linearity begins to break down close to the saturation limit (≈ 4096 counts), which is to be expected and is accounted for when the images taken at different exposure times are combined for each polarization angle (Section 2.2.4). The linearity of the sensor was quantified using Equation 2:

$$\text{Linearity}\,(\%) = \frac{(\text{MPD} + \text{MND})}{\text{MI}} \times 100, \qquad (2)$$

where MPD, MND, and MI are the maximum positive deviation, maximum negative deviation, and maximum intensity, respectively. The maximum positive and negative deviations were found from the line of best fit. This calculation was performed twice – once including the last data point where the linearity begins to break down, and a second time without including the aforementioned data point. These calculations result in linearities of 2.99% and 0.96%, respectively. Both of these values are excellent linearities since most CMOS sensors have linearities on the order of several percent (Wang and Theuwissen, 2017).

2.2.2. Flat-Field and Dark-Frame Correction

Five flat-field images were taken at an exposure time of 0.01 s for each polarization angle using an integrating sphere. A master flat-field image was then produced for each polarization angle using the open-source plugin AstroImageJ – an example of one of these is seen in Figure 5 along with an intensity profile taken at the midpoint of the image.

Figure 5 Master flat-field image for a polarization angle of 0° (top) and a normalized intensity profile taken at the midpoint of the image shown by the red horizontal line (bottom).
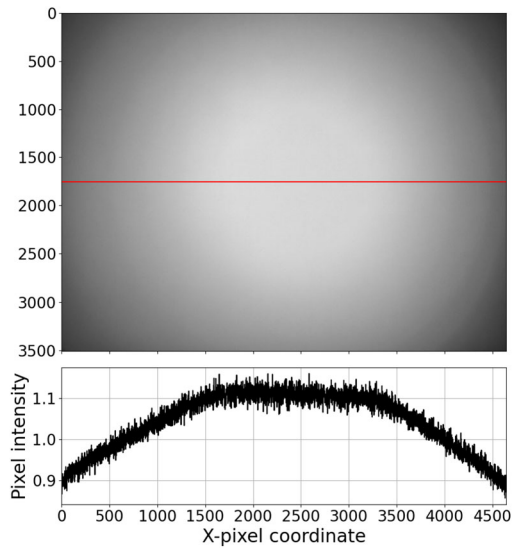

Two different types of dark-field images were attempted: first, setting the exposure time of the camera to zero and taking several pictures to obtain an average; and secondly, blocking the front of the instrument with the lens cap and running the full eclipse sequence five times. Unfortunately, the Atik Horizon II has a minimum exposure time of 18 µs so the first method was not able to be carried out. For the second method, the instrument was taken to a dark room with the lens cap taped over the lens. Several dark frames were taken in this way for each polarization angle and exposure time used in the eclipse sequence. It is expected that the mean values of the intensity (along with their standard deviations) should be similar for each polarization angle and exposure time and this is indeed what was seen. Figure 6 shows the dark noise, σ_{dark}, calculated by taking the average standard deviation of all dark frames taken at each exposure time and polarization angle. It is clear that pixels in the detector follow the same pattern and behave uniformly across all polarization angles.

Once the master flat-field and dark-frame images were produced, the raw eclipse images were calibrated using Equation 3:

$$C_{\theta,t} = \frac{(R_{\theta,t} - D_t) \times m}{(F_\theta - D_t)}, \qquad (3)$$

where $C_{\theta,t}$ is the reduced image, $R_{\theta,t}$ is the raw image taken at a specific polarization angle (θ) and exposure time (t), D_t is the dark frame for that particular exposure, F_θ is the flat field for that particular polarization angle, and m is the image-averaged value of $(F_\theta - D_t)$. At this stage, the scale of the image was calculated. The radius of the Moon was found to be 255.5 ± 0.5 pixels by fitting a circle to points plotted along the lunar limb using ImageJ. One of the lowest exposure images was used to obtain this radius in order to reduce the brightness from the lower corona to obtain the most accurate value possible. The Moon's apparent radius at the time of the eclipse was found to be $1000.145''$ using the Stellarium software (Zotti et al., 2021), therefore, the full-resolution images provided a spatial resolution of 3.92 ± 0.01 arcsec/pixel.
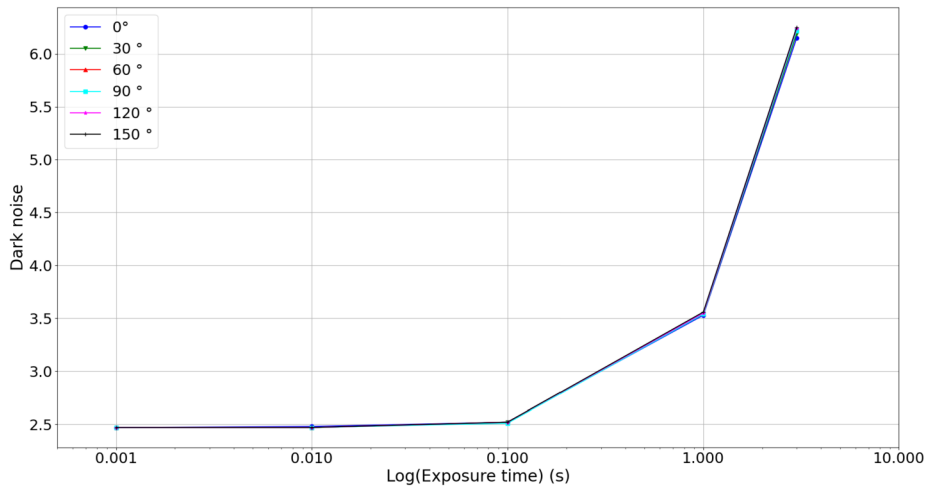
Figure 6 Average dark noise for all polarization angles as a function of the exposure time.

2.2.3. Image Coalignment

After the initial calibration of the raw images with the dark and flat frames, they were coaligned before the images with different exposure times could be combined. This step was crucial because, although a motorized tracking mount was used to track the solar center, there were still some factors that needed to be accounted for and corrected. The two main factors were the high winds at ground level throughout the eclipse and the fact that the Moon was moving with respect to the Sun. The effect of the wind on the tracking mount can be seen in Figures 7 and 8. As discussed in Section 1, there are several different methods of coaligning eclipse images such as the use of phase correlation (e.g. Druckmüller, 2009) or by using the positions of stars visible in the exposures (e.g. Bemporad, 2020). In this study, three stars were visible in the images taken at longer exposure times (see Figure 7) and were identified using Stellarium to be HD 157056 (star 1), HD 157792 (star 2), and HD 158643 (star 3), respectively. The images were initially coaligned using the brightest of these stars (HD 157056), which is star 1 in Figure 7, since its drift in both the x- and y-direction was fairly consistent (Figures 7 and 8). For the shorter exposure images, where the stars were not visible, it was assumed that the star did not move much relative to its position in the 1 and 3 s exposures. Shifts in both the x- and y-pixels were calculated for each image, based on their respective exposure times, using the equations found, in Figure 8 and all of the images were coaligned accordingly. The images were then rebinned through 8×8 pixel averaging to improve the signal quality, which reduced the resolution of the images to 31.25 ± 0.01 arcsec/pixel.

2.2.4. Image Combination

The next step was to combine all the images of different exposure times for each individual polarization angle. First, all negative pixel values were set to zero and the images were normalized by their respective exposure times (DN/s) using Equation 4:

$$I'_p = \frac{I_p}{\Delta t_e},$$

(4)
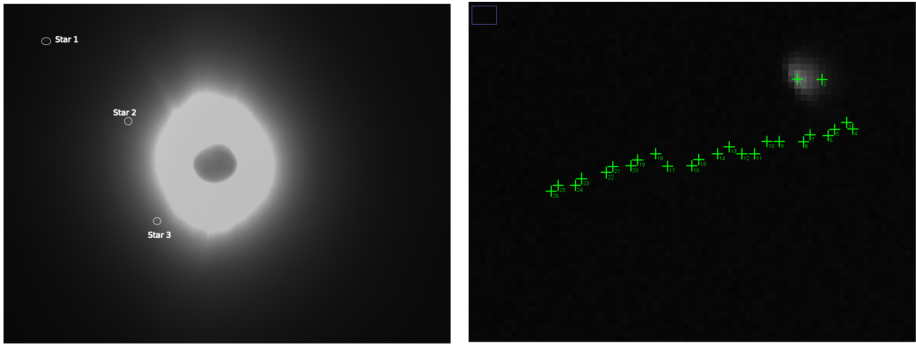
Figure 7 Left: Locations of the three visible stars in a 3 s exposure time image. Right: Locations of the brightest pixel in star 1 for all 1 and 3 s exposures.
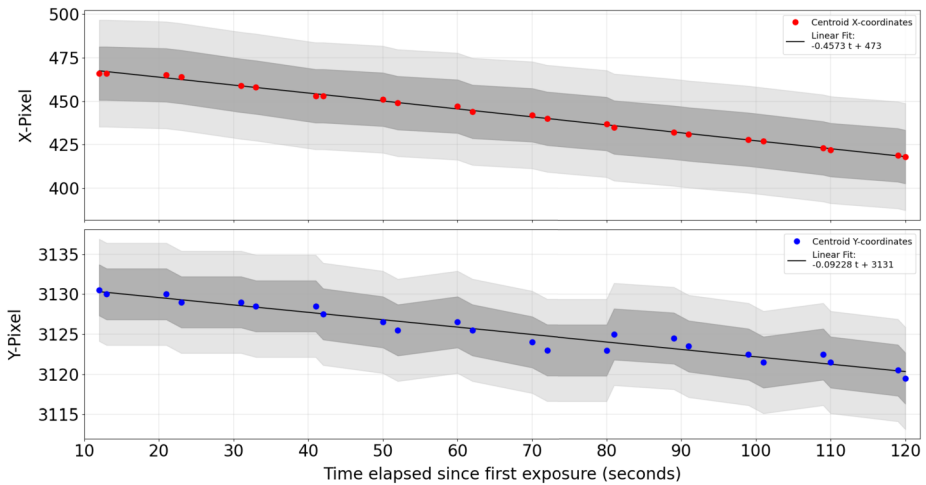
Figure 8 Pixel drifts in both the x- and y-coordinates for star 1. The data points represent the pixel coordinate of the brightest pixel during the 1 and 3 s exposures. The darker and lighter shaded regions show one and two standard deviations, respectively.

where I'_p is the pixel intensity (I_p) for each polarization angle p, normalized by exposure time (Δt_e). Since the eclipse images have a very high dynamic range between the brightest and darkest pixels, they need to be combined together in a way that takes the pixel value itself into account. In the shorter exposure images, the inner coronal signal is strong but the outer coronal signal is too weak, whereas, in the longer-exposure images, the outer coronal signal is strong but the inner corona is overexposed. Thus, the images need to be combined in such a way that the inner and outer corona are adequately exposed in the final image. This is done by using a signal-to-noise ratio (SNR) cut based on the square root of the intensity, thus providing a lower boundary wherein any pixels with a value less than this threshold are excluded. The SNR cut used in this work was $I > \sqrt{I}$ where I is the intensity of the pixel. An upper threshold of 3900 counts is also used since the linearity of the CMOS sensor breaks down around this value (see Figure 4). This process was done for each image taken
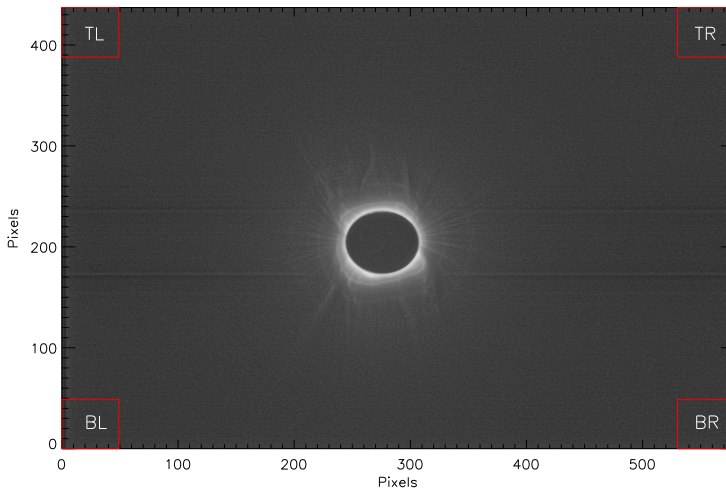
Figure 9   Location of each box used to determine the sky brightness overlaid on the combined 0° image. The image has not been rotated so that solar north aligns with the top of the image. L, T, B, and R correspond to the left, top, bottom, and right sides of the image, respectively.

at a given polarization angle, which means that each composite image consists of two sets of different exposure times.

### 2.2.5. Sky-Brightness Removal

During a TSE, the local sky brightness is significantly lowered to $\approx 10^{-9} - 10^{-10}$ B$_\odot$ that allows unmatched VL observations of the corona out to greater heliocentric heights than without a TSE. However, the sky brightness during a TSE is not negligible and must be removed from the data. As Figure 9 shows, a box was defined in each corner of each combined TSE image. There is a considerable amount of noise present in the image as a result of the poor weather conditions, despite the rebinning to improve the signal-to-noise ratio. There is also an optical artifact that takes the form of two parallel lines spanning the width of the image, the cause of which is unknown but is most probably instrumental. The mean intensity in each box was then calculated and the process was repeated for each polarizer angle. The result of this can be seen in Figure 10 which seems to show that the intensity at the right-hand side of the image (corresponding to solar north) is greater than that of the left-hand side (corresponding to solar south). A map is then created to estimate the sky brightness at each point in the image by interpolating the mean counts between each of the four boxes for each polarizer angle separately. Two examples of these interpolated sky-brightness maps are shown in Figure 11 for 0° and 90°. The polarization of the background sky lies at around 10% of the overall polarization of the image and this component is subsequently removed as a result of this sky-brightness removal step. Finally, the F-coronal component has a noticeable impact on *pB* data from heliocentric heights of $\approx 2.5 - 3.0$ R$_\odot$ (Boe et al., 2021b) but since this study limited observations to a heliocentric height of 1.5 R$_\odot$, the F-coronal component can be neglected at such low heights.

2.2.6. Determining the Polarized Brightness

A standard inversion method used to acquire coronal electron densities was initially developed by van de Hulst (1950) and further developed by Newkirk (1967), Saito, Poland, and
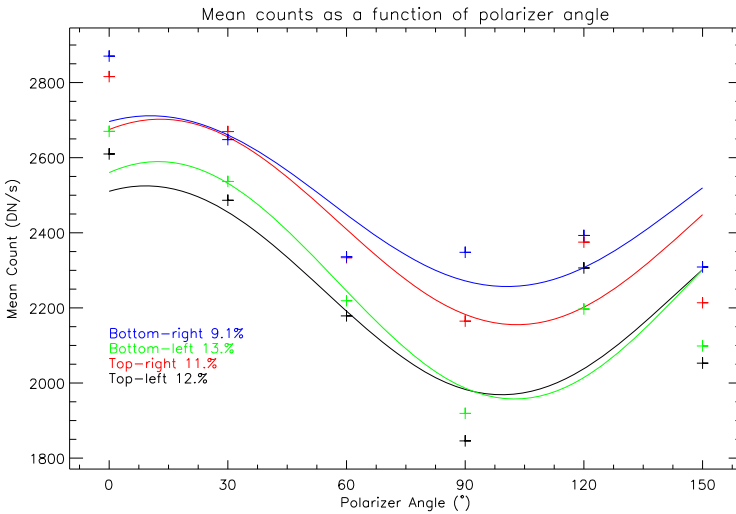
Figure 10 Mean intensity for each box in Figure 9 at each polarizer angle. The fit to Equation 5 is shown as a solid line for each of the four boxes where the results from the top-left, top-right, bottom-left, and bottom-right boxes are shown in black, red, green, and blue, respectively. The mean polarization of each box is also expressed as a percentage of the total polarization.
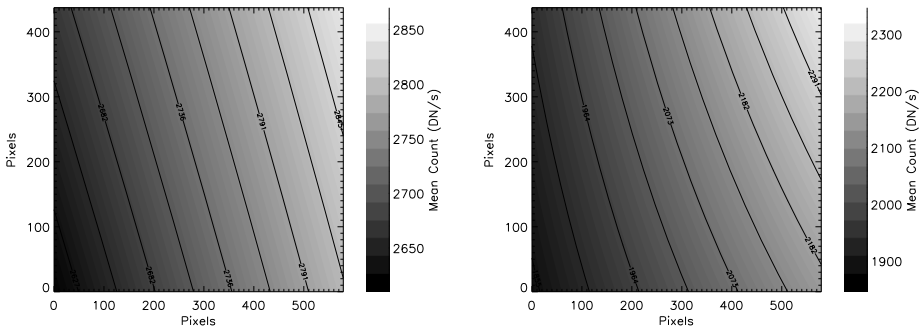
Figure 11 Examples of interpolated sky-brightness maps subtracted from the respective TSE images for polarizer orientation angles of 0° (left) and 90° (right).

Munro (1977), Hayes, Vourlidas, and Howard (2001), and Quémerais and Lamy (2002), among others. The original model assumes both spherical symmetry and that the pB is produced purely by the Thomson scattering of photospheric light from free coronal electrons and it is proportional to the integrated LOS density of the electrons, as shown in Equation 1. Most similar studies use three or four different polarization angles to determine the pB – typically −60°, 0°, 60° (Hanaoka, Sakai, and Takahashi, 2021), and 0°, 45°, 90°, 135° (Vorobiev et al., 2020). However, CIP captured images taken at different exposure times for six different polarization angles (0°, 30°, 60°, 90°, 120°, and 150°). As a result, in order to invert the calibrated intensities to find the pB at each pixel, an approach involving least-squares fitting was used. For a polarizer angle, θ_i, where $i = 0, 1, 2, \ldots, n-1$ (with $n = 6$

for this study), the measured intensity, I_i, is described by Equation 5:

$$I_i = I_0 + a \cos 2\theta_i + b \sin 2\theta_i, \tag{5}$$

where the coefficients to be fitted are the unpolarized background intensity, I_0, and the polarized components, a and b. The polarized brightness is then given by

$$pB = \sqrt{a^2 + b^2}. \tag{6}$$

In order to find a solution for I_0 and pB at each pixel, the squared sum is then minimized as follows:

$$\sum_{i=0}^{n-1} [I_i - (I_0 + a \cos 2\theta_i + b \sin 2\theta_i)]^2. \tag{7}$$

This least-squares fitting method was tested against the standard Mueller matrix-inversion method for three polarization angles (0°, 60°, and 120°) and it agreed within a few percent. As a result, CIP can theoretically take images of the corona for any number of polarizer angles in the future.

2.2.7. Relative Radiometric Calibration

A relative radiometric calibration step converts the polarized brightness measured by CIP (recorded as DN/s) to units relative to the mean solar brightness (MSB). The instrument used in this step was the *Mauna Loa Solar Observatory's* (MLSO) COSMO *K-Coronagraph* (doi:10.5065/D69G5JV8) that provides *pB* data with a field-of-view from 1.05 to ≈ 3 R$_\odot$ and a spatial resolution of 11.3". The 10-min averaged K-Cor data was used for this calibration step with the first observation occurring at 17:56:41 UTC and the last at 18:10:20 UTC. Figure 12 shows the 10-minute averaged *pB* observations taken by MLSO/K-Cor instrument on the day of the TSE, processed using the Multi-scale Gaussian Normalization technique (Morgan and Druckmüller, 2014) in order to enhance the fine-scale coronal structure, and the concentric rings represent heliocentric heights of 1.0, 1.5, 2.0, and 2.5 R$_\odot$, respectively. It is clear that consistent *pB* data is restricted to ≈ 1.7 R$_\odot$ with the data extending further out in the equatorial regions. As a result, the relative radiometric calibration in this study was limited to a heliocentric height of 1.5 R$_\odot$.

The images from both CIP and K-Cor are then coaligned and an intensity profile is taken for a thin slice of the corona at a specified height for both images. Some examples of these intensity profiles can be seen in Figure 13 for a range of heliocentric heights. A calibration factor is temporarily applied to the CIP data in order to visualize both latitudinal profiles on the same axis scale, which is denoted in each plot as CF. The mean ratio of the data from both instruments is then computed at intervals of 0.025 R$_\odot$ between 1.1 and 1.5 R$_\odot$ and these values are shown in Figure 14. This linear increase in the intensity ratio with height is then applied to the TSE data, thus converting the *pB* observations taken with CIP from units of DN/s to units of solar brightness ($B_\odot$). A crosscorrelation was also performed on the intensity profiles to find the angle needed to rotate the CIP data in order to align it with that taken by K-Cor (i.e. solar north upwards).

Figure 12 10-min averaged *pB* observations taken by MLSO/K-Cor instrument on the day of the eclipse, processed using the Multi-scale Gaussian Normalization technique, with the concentric circles corresponding to heliocentric heights of 1.0, 1.5, 2.0, and 2.5 $R_\odot$, respectively.
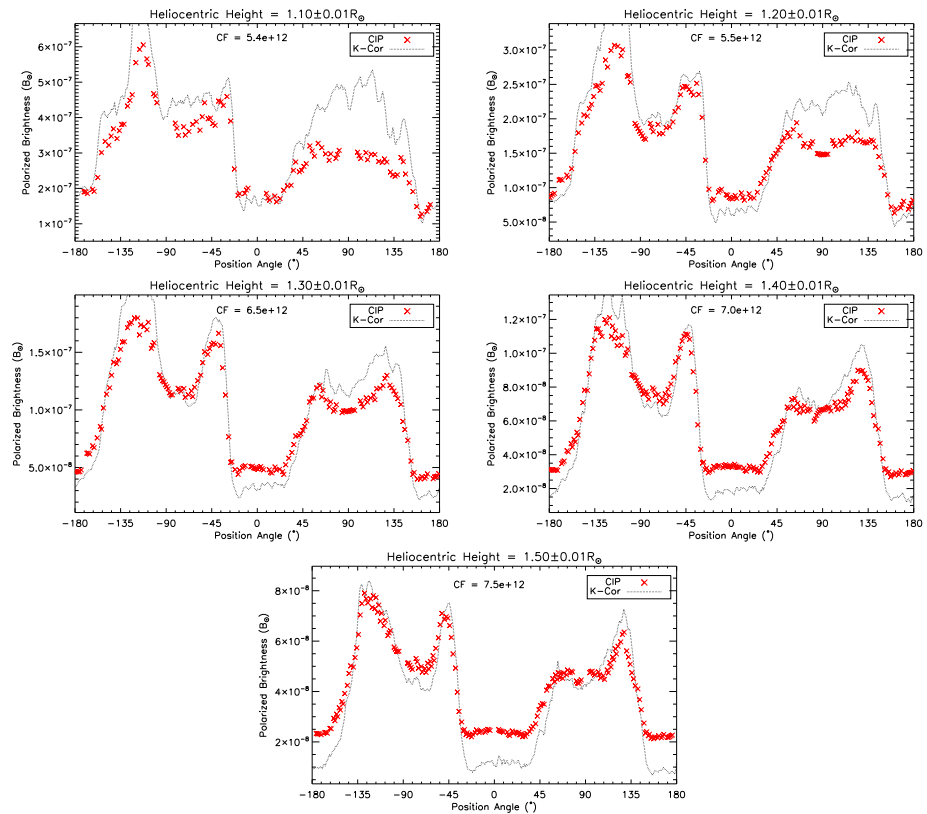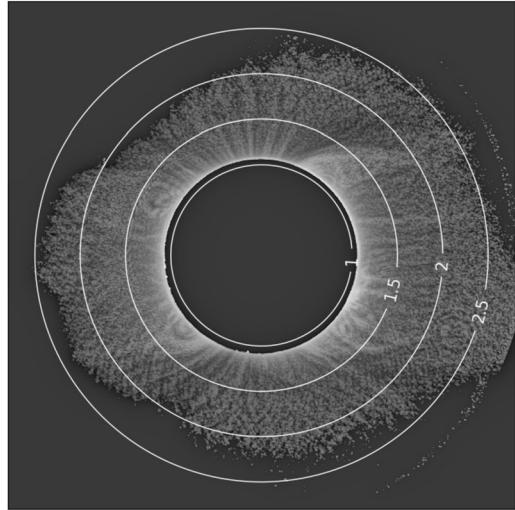

Figure 13 Latitudinal distribution of intensity profiles from both CIP (red) and K-Cor (black) for a range of heliocentric heights. A calibration factor (CF), noted in each plot, is temporarily applied to the CIP data in order to see both profiles on the same axis scale.

Figure 14 Mean intensity ratio between the CIP and K-Cor intensity profiles for each height interval (black) along with the linear fit used to perform the relative radiometric calibration of the TSE data (red).
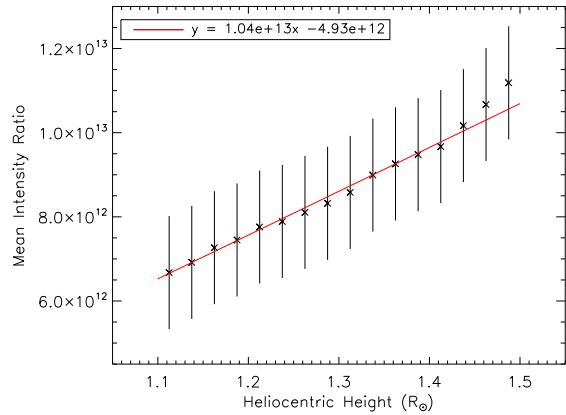
Figure 15 Final MGN-processed *pB* image of the 14 December 2020 TSE after relative radiometric calibration with respect to MLSO/K-Cor.
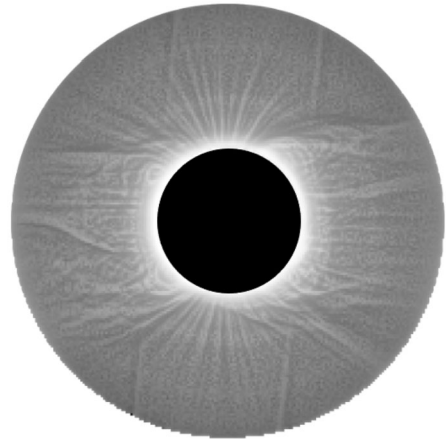

3. Results

Figure 15 shows the final calibrated *pB* image of the 14 December 2020 TSE. It has been further processed using the Multi-Scale Gaussian Normalization (MGN) technique to enhance the fine-scale coronal detail. Due to the poor viewing conditions at the observation site adversely affecting the data, the data analysis has been limited to a heliocentric height of 1.5 $R_\odot$, but the image in Figure 15 has been extended out to 2 $R_\odot$ to show more of the corona.

Figure 16 shows a comparison of *pB* data as a function of heliocentric height for the north polar coronal hole and west equatorial streamer chosen for this study (at position angles 12° and 245° counterclockwise from solar north, respectively). As would be expected, the *pB* is highest in the solar equatorial region and lower in the polar region. It is clear to see that the relative radiometric calibration with respect to MLSO/K-Cor is optimal at the equator but the polar *pB* observed by CIP is still greater than that of K-Cor. This is believed to be due to the poor weather conditions at the time of observation having a greater effect on the fainter coronal signal in the polar regions. However, the K-Cor instrument has to contend with a much higher sky brightness in comparison to TSE observations and Boe et al. (2021a) found that K-Cor data were unreliable as low as ≈ 1.2 or 1.3 $R_\odot$ in the coronal hole regions

Figure 16 Calibrated and corrected *pB* profiles from CIP (black) and K-Cor (red) for both the polar coronal hole and equatorial streamer.
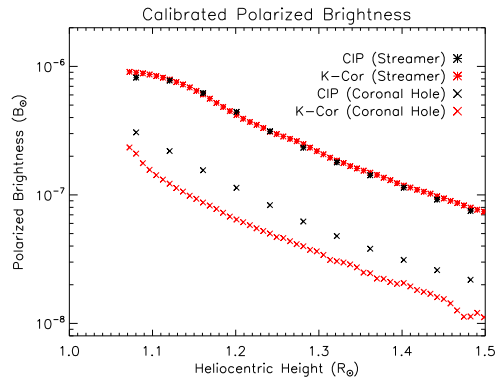

Figure 17 Latitudinal distribution of *pB* for the heliocentric heights of 1.2 (black), 1.3 (red), 1.4 (blue), and 1.5 $R_\odot$ (green). Vertical dotted lines are included to represent the position angles for the polar coronal hole (left), CME (middle), and equatorial streamer (right).
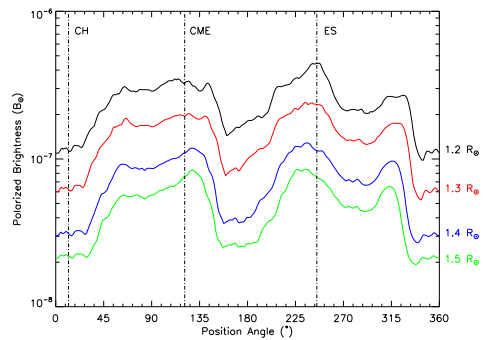
when compared with TSE data, which could also explain the discrepancy between the two instruments. There could also be some wavelength-dependent effect causing the discrepancy since CIP's central wavelength is at 520 nm and K-Cor is centered in the far red ($\approx$ 800 nm). It is, therefore, difficult to say with absolute certainty what is causing the discrepancy.

Figure 17 shows the latitudinal distribution of the *pB* for heliocentric heights of 1.2, 1.3, 1.4, and 1.5 $R_\odot$ in black, red, blue, and green, respectively. The *pB* decreases with increasing distance from the limb, which is to be expected, and all four latitudinal distributions have a similar shape, but there is a noticeable offset between corresponding maxima and minima as heliocentric height increases. The dotted vertical lines represent the position angles at which the densities are calculated for the polar coronal hole and the equatorial streamer, as well as the position angle for the CME where its presence becomes increasingly apparent in the 1.4 and 1.5 $R_\odot$ *pB* distributions.

Figure 18 shows the coronal electron densities, derived by inverting the *pB*, as a function of heliocentric height for both the polar coronal hole (left) and equatorial streamer (right). Both plots also show comparisons to data from previous works that agree very well with the data from this study. As expected, the density of the streamer is greater than that of the coronal hole by an average factor of $\approx$ 4 between $1.1 - 1.5$ $R_\odot$. For the coronal-hole comparison, density profiles from Baumbach (1937), Doyle, Teriaca, and Banerjee (1999), and Guhathakurta et al. (1999) were used. The latter two in particular were selected because they represent observations of polar coronal holes taken at the start of Solar Cycle 24 (solar minimum) and, since the 2020 TSE occurred exactly a year after the start of Solar Cycle 25, they are reasonable comparisons to make. For the equatorial streamer, the densities obtained in this study are compared with Gibson et al. (1999), Liang et al. (2022), and Gallagher
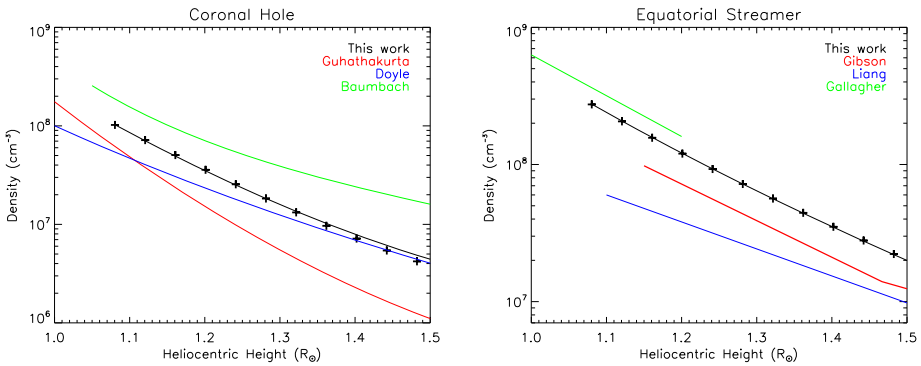
Figure 18   Coronal electron densities as a function of heliocentric height for the coronal hole (left) compared with Baumbach (1937), Doyle, Teriaca, and Banerjee (1999), and Guhathakurta et al. (1999), and the equatorial streamer (right) compared with Gibson et al. (1999), Liang et al. (2022), and Gallagher et al. (1999). The black data points show the densities acquired by inverting the *pB* and the solid black line shows the fit to Equation 9.

et al. (1999). Again, these are reasonable comparisons to make since the compared works represent observations of a streamer (Gibson et al., 1999) and equatorial regions (Liang et al., 2022; Gallagher et al., 1999) taken at or near solar minimum.

4. Discussion

4.1. Number of Polarizer Angles

Typically, similar studies and space-based coronagraphs use polarizer angles of $0°$, $60°$, and $120°$ to infer the coronal electron density. As mentioned previously, CIP is designed to efficiently take polarized observations for any number of predefined polarizer angles. For this study, six polarizer angles were chosen in an attempt to see if increasing the number of polarizer angles leads to better constraints on the *pB* observations and the inferred coronal electron densities. Figure 19 shows the mean percentage difference between the coronal electron densities derived using all six polarizer angles (henceforth referred to as angle set A) and only the $0°$, $60°$, and $120°$ polarizer angles (angle set B) with the error bars representing the standard error in the mean. The difference is shown as a function of the position angle between the heliocentric heights $1.1 - 1.5$ R$_\odot$ and ranges from -12.8% to 9.44% with the overall mean at 0.56%. For the position angles chosen to represent the coronal hole and equatorial streamer, the mean difference is -8.26% and 8.04%, respectively. This is a very important result. The difference, which is on the order of 10%, implies that the accuracy of *pB* observations can benefit greatly from increasing the number of polarizer angles, with direct improvements to density diagnostics. This error has significant implications for the design and development of future TSE observing instruments and, more importantly, space-based coronagraphs.

Figure 20 shows the difference in density between both angle sets A (red) and B (black) as a function of heliocentric height for both the coronal hole (left) and equatorial streamer (right). It is clear to see that the densities found using set A (all polarizer angles) are lower in the coronal hole and higher in the equatorial streamer in comparison to those found using only set B ($0°$, $60°$, $120°$). Furthermore, the difference between the two calculated densities

Figure 19 Mean difference between the coronal electron densities derived using all six polarizer angles (angle set A) and only the 0°, 60°, and 120° polarizer angles (angle set B). The mean difference ranges from ≈ −13% to 10% and the mean in the difference is also shown (red line). The error bars show the standard error in the mean.
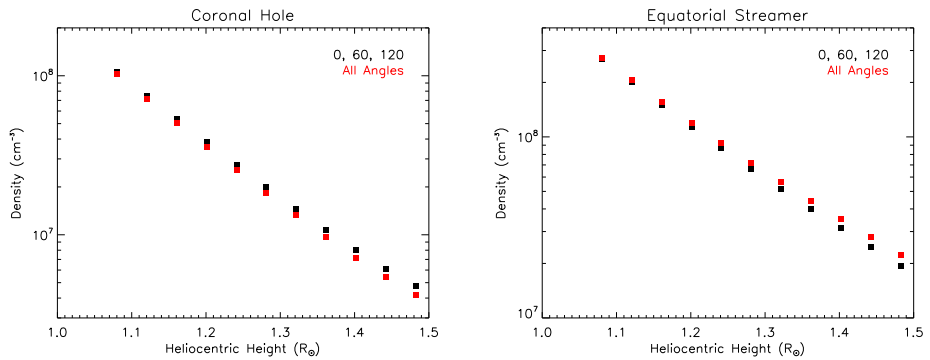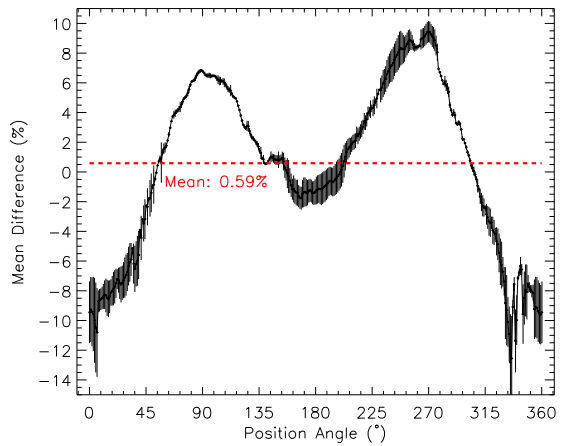
Figure 20 Difference in coronal electron densities between using *pB* data from angle sets A (red) and B (black) for both the coronal hole and equatorial streamer.

clearly becomes greater with increasing heliocentric height, which is shown more clearly in Figure 21. Since the difference increases with increasing heliocentric height, it is unfortunate that the weather conditions on the day of the TSE were suboptimal because it would be interesting to see how this difference evolves beyond the inner coronal region. However, the existence of this difference confirms that changing the number of polarizer angles used does provide a better constraint on the inferred coronal electron densities, particularly for heliocentric heights above ≈ 1.5 $R_\odot$. This result has even more important implications for space-based coronagraphs, such as LASCO C2 whose field-of-view begins at 1.5 $R_\odot$ and extends out to 6 $R_\odot$. For the remainder of the analysis of these results, set A (all polarizer angles) was used.

4.2. Radial Density Fitting

Several studies (Saito, Poland, and Munro, 1977; Guhathakurta et al., 1999; Hayes, Vourl-idas, and Howard, 2001; Thernisien and Howard, 2006) state that the radial dependence of the coronal electron density can be expressed in the form of a polynomial:

$$N_e(r) = \Sigma_i \alpha_i r^{-i}, \tag{8}$$

Figure 21 Mean difference (expressed as a percentage) between using *pB* data from angle sets A and B for both the coronal hole (black) and equatorial streamer (red) with the error bars representing one standard deviation in both cases.
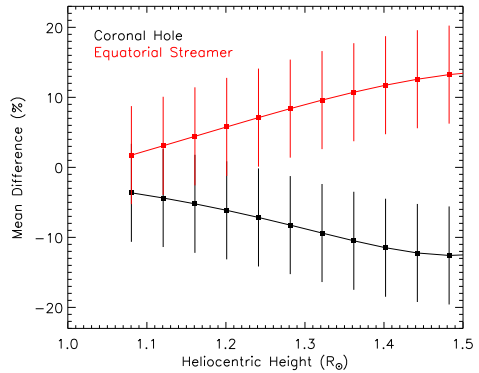
Table 1 Coefficients for Equation 9.

	a	b	c	d	e	f
Coronal Hole	1.12×10^6	0.107	2.27×10^8	10.4	1.50×10^8	560
Equatorial Streamer	8.56×10^5	83.8	3.80×10^7	7.91	4.70×10^8	7.91

where r is given in solar radii and α and β are coefficients fitted to the data. Since the analysis of the data obtained in this study extended from below $\approx 1.1 - 1.5\ \mathrm{R_\odot}$, three terms are sufficient to provide a good fit to the data, thus, the equation used to fit the data and determine the coefficients was:

$$N_e(r) = ar^{-b} + cr^{-d} + er^{-f}. \tag{9}$$

The coefficients for both coronal features of interest are shown in Table 1 and they agree well with previous studies.

5. Conclusion

The primary aim of this study was to present a new design for a lightweight polarization instrument capable of observing using more polarization angles than is typically used, called the *Coronal Imaging Polarizer* (CIP). The instrument was designed and built at Aberystwyth University to observe the polarized brightness of the solar corona during the 14 December 2020 TSE for six orientation angles of the linear polarizer. Due to the design of the instrument, it is very easy to increase or decrease the number of polarization angles depending on the time available during the totality phase of an eclipse. One of the main design elements of CIP was that it would be lightweight in order to be easily transported to an observing site. This element was not only met but was also needed as the team had to relocate to a new observing site on the morning of the eclipse. The new site was a few hours' drive from the original site and with the instrument itself weighing only $\approx 1.59\ \mathrm{kg}$, the bulk of the transporting was due to the tripod and tracking mount. Consequently, the entire instrument was easily transported and the simplicity of the design meant that the team could set it up very quickly at the new observing site. However, the weather conditions at the new site still impacted the data – primarily the strong gusts of wind that can be clearly seen in Figure 7,

along with airborne dust and high humidity. The instrument was also designed to capture data fully autonomously and efficiently and, again, this aim was met.

The raw VL images were successfully corrected using flat-field and dark frame subtraction (see Section 2.2.2) and the corrected images were then manually coaligned by tracking the drift of a star in the background of the data throughout the duration of totality (see Section 2.2.3). The images were then rebinned to be 8×8 times smaller in order to improve the signal-to-noise ratio that might not be needed in future eclipses given better viewing conditions. The images of different exposure times were combined by using a simple signal-to-noise ratio cut to create composite images of the eclipse for each individual angle of polarization (see Section 2.2.4). These composite images were then combined to give the pB image using a simple least-squares fitting method (see Section 2.2.6) and relative radiometric calibration was successfully done by crosscalibration with MLSO/K-COR (see Section 2.2.7). The final pB image was then inverted, assuming a locally spherically symmetric corona, to produce radial density profiles for a polar coronal hole and an equatorial streamer. These densities were then compared with previous studies and were found to be in good agreement (see Section 3). The key finding of this study was the effect that varying the number of polarizer angles has on the inferred coronal electron densities. Densities were inferred for two datasets: one consisting of images taken at all six polarizer angles and the other with only three polarizer angles, which resulted in a difference of approximately $\pm 10\%$ in the densities. It is hoped that CIP can be sent to observe future TSEs to provide better quality constraints on pB and coronal electron densities and build upon the results of this study, particularly with regard to studying the impact of more polarization angles on the quality of TSE data. The authors plan to observe the "Great North American Eclipse" on 8 April 2024 with CIP but using 12 polarizer angles instead of 6 due to an extended totality of over 4 min. This should help provide better constraints on the effect of increasing the number of polarizer angles on the inferred coronal electron densities.

Author contributions L.E. wrote the main manuscript text and performed the majority of the data analysis and processing. K.B., B.R., and G.M. collected the data at the eclipse. T.F. wrote the automation code for the instrument to take the data. T.K. contributed to the mathematical formulation of the calculation of pB. M.G. contributed to the design of the instrument and assembled it. H.M. contributed to the writing of the manuscript, data analysis, image processing, and reviewed the manuscript.

Data Availability The data generated and/or analyzed during the current study are available from the corresponding author upon reasonable request. Some of the pB data and coronal images used in this work are courtesy of the Mauna Loa Solar Observatory, operated by the High Altitude Observatory, as part of the National Center for Atmospheric Research (NCAR). NCAR is supported by the National Science Foundation.

Declarations

Competing interests The authors declare no competing interests.

References

Baumbach, S.: 1937, Strahlung, ergiebigkeit und elektronendichte der sonnenkorona. *Astron. Nachr.* **263**(6), 121. DOI. https://onlinelibrary.wiley.com/doi/abs/10.1002/asna.19372630602.

Bemporad, A.: 2020, Coronal electron densities derived with images acquired during the 2017 August 21 total solar eclipse. *Astrophys. J.* **904**(2), 178. DOI. ADS.

Boe, B., Habbal, S., Downs, C., Druckmuller, M.: 2021a, A new color-based method for K- and F-corona extraction. In: *AGU Fall Meeting Abs. 2021*. SH15D. ADS.

Boe, B., Habbal, S., Downs, C., Druckmuller, M.: 2021b, The color and brightness of the F-corona inferred from the 2019 July 2 total solar eclipse. *Astrophys. J.* **912**(1), 44. DOI. ADS.

Boe, B., Yamashiro, B., Druckmüller, M., Habbal, S.: 2021c, The double-bubble coronal mass ejection of the 2020 December 14 total solar eclipse. *Astrophys. J. Lett.* **914**(2), L39. DOI. ADS.

Brueckner, G.E., Howard, R.A., Koomen, M.J., Korendyke, C.M., Michels, D.J., Moses, J.D., Socker, D.G., Dere, K.P., Lamy, P.L., Llebaria, A., Bout, M.V., Schwenn, R., Simnett, G.M., Bedford, D.K., Eyles, C.J.: 1995, The Large Angle Spectroscopic Coronagraph (LASCO). *Solar Phys.* **162**(1 – 2), 357. DOI. ADS.

Byrne, J.P., Morgan, H., Habbal, S.R., Gallagher, P.T.: 2012, Automatic detection and tracking of coronal mass ejections. II. Multiscale filtering of coronagraph images. *Astrophys. J.* **752**(2), 145. DOI. ADS.

Calbert, R., Beard, D.B.: 1972, The F and K components of the solar corona. *Astrophys. J.* **176**, 497. DOI. ADS.

De Pontieu, B., McIntosh, S.W., Hansteen, V.H., Schrijver, C.J.: 2009, Observing the roots of solar coronal heating – in the chromosphere. *Astrophys. J. Lett.* **701**(1), L1. DOI. ADS.

Del Zanna, G., Samra, J., Monaghan, A., Madsen, C., Bryans, P., DeLuca, E., Mason, H., Berkey, B., de Wijn, A., Rivera, Y.J.: 2023, Coronal densities, temperatures, and abundances during the 2019 total solar eclipse: the role of multiwavelength observations in coronal plasma characterization. *Astrophys. J. Suppl.* **265**(1), 11. DOI. ADS.

Domingo, V., Fleck, B., Poland, A.I.: 1995, The SOHO mission: an overview. *Solar Phys.* **162**(1 – 2), 1. DOI. ADS.

Doyle, J.G., Teriaca, L., Banerjee, D.: 1999, Coronal hole diagnostics out to 8R$_{sun}$. *Astron. Astrophys.* **349**, 956. ADS.

Druckmüller, M.: 2009, Phase correlation method for the alignment of total solar eclipse images. *Astrophys. J.* **706**(2), 1605. DOI. ADS.

Druckmüller, M.: 2013, A noise adaptive fuzzy equalization method for processing solar extreme ultraviolet images. *Astrophys. J. Suppl.* **207**(2), 25. DOI. ADS.

Druckmüllerová, H., Morgan, H., Habbal, S.R.: 2011, Enhancing coronal structures with the Fourier normalizing-radial-graded filter. *Astrophys. J.* **737**(2), 88. DOI. ADS.

Dürst, J.: 1982, Two colour photometry and polarimetry of the solar corona of 16 February 1980. *Astron. Astrophys.* **112**, 241. ADS.

Fainshtein, V.G.: 2009, New method for separating K- and F-corona brightness based on LASCO/SOHO data. *Geomagn. Aeron.* **49**(7), 830. DOI. ADS.

Filippov, B., Koutchmy, S., Lefaudeux, N.: 2020, Solar total eclipse of 21 August 2017: study of the inner corona dynamical events leading to a CME. *Solar Phys.* **295**(2), 24. DOI. ADS.

Gallagher, P.T., Mathioudakis, M., Keenan, F.P., Phillips, K.J.H., Tsinganos, K.: 1999, The radial and angular variation of the electron density in the solar corona. *Astrophys. J. Lett.* **524**(2), L133. DOI. ADS.

Gibson, S.E., Fludra, A., Bagenal, F., Biesecker, D., del Zanna, G., Bromage, B.: 1999, Solar minimum streamer densities and temperatures using whole Sun month coordinated data sets. *J. Geophys. Res.* **104**(A5), 9691. DOI. ADS.

Gopalswamy, N., Yashiro, S., Michalek, G., Stenborg, G., Vourlidas, A., Freeland, S., Howard, R.: 2009, The SOHO/LASCO CME catalog. *Earth Moon Planets* **104**(1 – 4), 295. DOI. ADS.

Guhathakurta, M., Fludra, A., Gibson, S.E., Biesecker, D., Fisher, R.: 1999, Physical properties of a coronal hole from a coronal diagnostic spectrometer, Mauna Loa Coronagraph, and LASCO observations during the whole Sun month. *J. Geophys. Res.* **104**(A5), 9801. DOI. ADS.

Habbal, S.R.: 2020, Total solar eclipse observations: a treasure trove from the source and acceleration regions of the solar wind. *J. Phys. Conf. Ser.* **1620**, 012006. DOI. ADS.

Habbal, S.R., Morgan, H., Johnson, J., Arndt, M.B., Daw, A., Jaeggli, S., Kuhn, J., Mickey, D.: 2007, Localized enhancements of Fe^{+10} density in the corona as observed in Fe XI 789.2 nm during the 2006 March 29 total solar eclipse. *Astrophys. J.* **663**(1), 598. DOI. ADS.

Habbal, S.R., Druckmüller, M., Morgan, H., Daw, A., Johnson, J., Ding, A., Arndt, M., Esser, R., Rušin, V., Scholl, I.: 2010, Mapping the distribution of electron temperature and Fe charge states in the corona with total solar eclipse observations. *Astrophys. J.* **708**(2), 1650. DOI. ADS.

Habbal, S.R., Druckmüller, M., Morgan, H., Ding, A., Johnson, J., Druckmüllerová, H., Daw, A., Arndt, M.B., Dietzel, M., Saken, J.: 2011, Thermodynamics of the solar corona and evolution of the solar magnetic field as inferred from the total solar eclipse observations of 2010 July 11. *Astrophys. J.* **734**(2), 120. DOI. ADS.

Hanaoka, Y., Sakai, Y., Takahashi, K.: 2021, Polarization of the corona observed during the 2017 and 2019 total solar eclipses. *Solar Phys.* **296**(11), 158. DOI. ADS.

Hanaoka, Y., Hasuo, R., Hirose, T., Ikeda, A.C., Ishibashi, T., Manago, N., Masuda, Y., Morita, S., Nakazawa, J., Ohgoe, O., Sakai, Y., Sasaki, K., Takahashi, K., Toi, T.: 2018, Solar coronal jets extending to high altitudes observed during the 2017 August 21 total eclipse. *Astrophys. J.* **860**(2), 142. DOI. ADS.

Hayes, A.P., Vourlidas, A., Howard, R.A.: 2001, Deriving the electron density of the solar corona from the inversion of total brightness measurements. *Astrophys. J.* **548**(2), 1081. DOI. ADS.

Hou, J., de Wijn, A.G., Tomczyk, S.: 2013, Design and measurement of the Stokes polarimeter for the COSMO K-coronagraph. *Astrophys. J.* **774**(1), 85. DOI. ADS.

Howard, R.A., Moses, J.D., Vourlidas, A., Newmark, J.S., Socker, D.G., Plunkett, S.P., Korendyke, C.M., Cook, J.W., Hurley, A., Davila, J.M., Thompson, W.T., St Cyr, O.C., Mentzell, E., Mehalick, K., Lemen, J.R., Wuelser, J.P., Duncan, D.W., Tarbell, T.D., Wolfson, C.J., Moore, A., Harrison, R.A., Waltham, N.R., Lang, J., Davis, C.J., Eyles, C.J., Mapson-Menard, H., Simnett, G.M., Halain, J.P., Defise, J.M., Mazy, E., Rochus, P., Mercier, R., Ravet, M.F., Delmotte, F., Auchere, F., Delaboudiniere, J.P., Bothmer, V., Deutsch, W., Wang, D., Rich, N., Cooper, S., Stephens, V., Maahs, G., Baugh, R., McMullin, D., Carter, T.: 2008, Sun Earth connection coronal and heliospheric investigation (SECCHI). *Space Sci. Rev.* **136**(1–4), 67. DOI. ADS.

Inhester, B.: 2015, Thomson scattering in the solar corona. arXiv e-prints. arXiv. ADS.

Jejčič, S., Heinzel, P., Zapiór, M., Druckmüller, M., Gunár, S., Kotrč, P.: 2014, Multi-wavelength eclipse observations of a quiescent prominence. *Solar Phys.* **289**(7), 2487. DOI. ADS.

Kaiser, M.L., Kucera, T.A., Davila, J.M., St. Cyr, O.C., Guhathakurta, M., Christian, E.: 2008, The STEREO mission: an introduction. *Space Sci. Rev.* **136**(1–4), 5. DOI. ADS.

Koutchmy, S., Baudin, F., Bocchialini, K., Daniel, J.-Y., Delaboudinière, J.-P., Golub, L., Lamy, P., Adjabshirizadeh, A.: 2004, The August 11th, 1999 CME. *Astron. Astrophys.* **420**, 709. DOI. ADS.

Lamy, P., Damé, L., Vivès, S., Zhukov, A.: 2010, ASPIICS: a giant coronagraph for the ESA/PROBA-3 formation flying mission. In: Oschmann, J., Jacobus, M., Clampin, M.C., MacEwen, H.A. (eds.) *Space Telescopes and Instrumentation 2010: Optical, Infrared, and Millimeter Wave*, *SPIE Conf Ser.* **7731**, 773118. DOI. ADS.

Lang, K.R.: 2010. Chapter 6: Perpetual change, Sun, NASA's cosmos, Tufts University. https://ase.tufts.edu/cosmos/print_images.asp?id=28.

Liang, Y., Qu, Z., Hao, L., Xu, Z., Zhong, Y.: 2022, Imaging-polarimetric properties of the white-light inner corona during the 2017 total solar eclipse. *Mon. Not. Roy. Astron. Soc.* DOI. ADS.

Lyot, B., Marshall, R.K.: 1933, The study of the solar corona without an eclipse. *J. R. Astron. Soc. Can.* **27**, 225. ADS.

McComas, D.J., Velli, M., Lewis, W.S., Acton, L.W., Balat-Pichelin, M., Bothmer, V., Dirling, R.B., Feldman, W.C., Gloeckler, G., Habbal, S.R., Hassler, D.M., Mann, I., Matthaeus, W.H., McNutt, R.L., Mewaldt, R.A., Murphy, N., Ofman, L., Sittler, E.C., Smith, C.W., Zurbuchen, T.H.: 2007, Understanding coronal heating and solar wind acceleration: case for in situ near-Sun measurements. *Rev. Geophys.* **45**(1), RG1004. DOI. ADS.

Morgan, H., Druckmüller, M.: 2014, Multi-scale Gaussian normalization for solar image processing. *Solar Phys.* **289**(8), 2945. DOI. ADS.

Morgan, H., Habbal, S.R.: 2007, The long-term stability of the visible F corona at heights of 3-6 R_⊙. *Astron. Astrophys.* **471**(2), L47. DOI. ADS.

Muro, G.D., Gunn, M., Fearn, S., Fearn, T., Morgan, H.: 2023, Visible emission line spectroscopy of the solar corona during the 2019 total solar eclipse. *PREPRINT (Version 1) available at Research Square*. DOI. https://www.researchsquare.com/article/rs-2538179/v1.

Newkirk, J.G.: 1967, Structure of the solar corona. *Annu. Rev. Astron. Astrophys.* **5**, 213. DOI. ADS.

Pasachoff, J.M., Rušin, V.: 2022, White-light coronal imaging at the 21 August 2017 total solar eclipse. *Solar Phys.* **297**(3), 28. DOI. ADS.

Patel, R., Majumdar, S., Pant, V., Banerjee, D.: 2022, A simple radial gradient filter for batch-processing of coronagraph images. *Solar Phys.* **297**(3), 27. DOI. ADS.

Qiang, Z., Bai, X., Ji, K., Liu, H., Shang, Z.: 2020, Enhancing coronal structures with radial local multi-scale filter. *New Astron.* **79**, 101383. DOI. ADS.

Quémerais, E., Lamy, P.: 2002, Two-dimensional electron density in the solar corona from inversion of white light images – application to SOHO/LASCO-C2 observations. *Astron. Astrophys.* **393**, 295. DOI. ADS.

Raju, A.K., Abhyankar, K.D.: 1986, Polarization and electron densities in the solar corona of 1980 February 16. *Bull. Astron. Soc. India* **14**, 217. ADS.

Reginald, N.L., Davila, J., St. Cyr, C.: 2009, Electron temperature maps of low solar corona: results from the total solar eclipse of 29 March 2006 in Libya. In: *AAS/Solar Physics Division Meeting* **40**, 14.03. ADS.

Reginald, N.L., Davila, J.M., St. Cyr, O.C., Rastaetter, L.: 2014, Evaluating the uncertainties in the electron temperature and radial speed measurements using white light corona eclipse observations. *Solar Phys.* **289**(6), 2021. DOI. ADS.

Saito, K., Poland, A.I., Munro, R.H.: 1977, A study of the background corona near solar minimum. *Solar Phys.* **55**(1), 121. DOI. ADS.

Sheeley, J.N.R., Wang, Y.-M.: 2014, Coronal inflows during the interval 1996-2014. *Astrophys. J.* **797**(1), 10. DOI. ADS.

Skomorovsky, V.I., Trifonov, V.D., Mashnich, G.P., Zagaynova, Y.S., Fainshtein, V.G., Kushtal, G.I., Chuprakov, S.A.: 2012, White-light observations and polarimetric analysis of the solar corona during the eclipse of 1 August 2008. *Solar Phys.* **277**(2), 267. DOI. ADS.

Strong, K., Viall, N., Schmelz, J., Saba, J.: 2017, Understanding space weather: part III: the Sun's domain. *Bull. Am. Meteorol. Soc.* **98**(12), 2593. DOI. ADS.

Thernisien, A.F., Howard, R.A.: 2006, Electron density modeling of a streamer using LASCO data of 2004 January and February. *Astrophys. J.* **642**(1), 523. DOI. ADS.

van de Hulst, H.C.: 1950, The electron density of the solar corona. *Bull. Astron. Inst. Neth.* **11**, 135. ADS.

Verroi, E., Frassetto, F., Naletto, G.: 2008, Analysis of diffraction from the occulter edges of a giant externally occulted solar coronagraph. *J. Opt. Soc. Am. A* **25**(1), 182. DOI. ADS.

Vorobiev, D., Ninkov, Z., Bernard, L., Brock, N.: 2020, Imaging polarimetry of the 2017 solar eclipse with the RIT polarization imaging camera. *Publ. Astron. Soc. Pac.* **132**(1008), 024202. DOI. ADS.

Wang, F., Theuwissen, A.: 2017, Linearity analysis of a CMOS image sensor. *Electron. Imaging* **29**, 84. DOI.

Zotti, G., Hoffmann, S.M., Wolf, A., Chéreau, F., Chéreau, G.: 2021, The simulated sky: stellarium for cultural astronomy research. *J. Skyscape Archaeol.* **6**(2), 221. DOI. https://journal.equinoxpub.com/JSA/article/view/17822.